Magnetic phase diagram for Fe 3 − x Mn x BO 5

F. Damay, J. Sottmann, F. Lainé, L. Chaix, M. Poienar, P. Beran, E. Elkaim, F. Fauth, L. Nataf, A. Guesdon, et al.

Magnetic phase diagram for $Fe_{3-x}Mn_xBO_5$

F. Damay,[1] J. Sottmann,[2] F. Lainé,[2] L. Chaix,[3] M. Poienar,[4] P. Beran,[5,6] E. Elkaim,[7] F. Fauth,[8] L. Nataf,[7] A. Guesdon,[2] A. Maignan,[2] and C. Martin[2]

[1] *Université Paris-Saclay, Laboratoire Léon Brillouin, CEA-CNRS UMR 12, 91191 Gif-sur-Yvette, France*
[2] *Normandie Univ, ENSICAEN, UNICAEN, CNRS, CRISMAT, 14000 Caen, France*
[3] *Laboratoire Léon Brillouin, CEA-CNRS UMR 12, Université Paris-Saclay, 91191 Gif-sur-Yvette, France*
[4] *National Institute for Research and Development in Electrochemistry and Condensed Matter, Str. Dr. A. Păunescu Podeanu, nr.144, 300569 Timişoara, Timiş, Romania*
[5] *Nuclear Physics Institute, 25068 REZ NEAR PRAGUE, Czech Republic*
[6] *European Spallation Source ERIC, Box 176, SE-221 00 Lund, Sweden*
[7] *Synchrotron Soleil, Saint-Aubin BP 48, 91192 GIF-sur-YVETTE Cedex, France*
[8] *CELLS ALBA Synchrotron, Carrer de la Llum 2-26, 08290 Cerdanyola del Vallès, BARCELONA, Spain*

(Dated: December 14, 2020)

The heterometallic ludwigite system $Fe_{3-x}Mn_xBO_5$ recently investigated for its ferroelectric properties has been studied using synchrotron and neutron diffraction, combined with XANES and magnetisation measurements. The results show that the *Pbam* crystal structure is preserved with little structural distortions up to x = 1.5, and that divalent Mn is substituted preferentially on the 3LL2 sub-lattice unit. As x increases, and up to Fe_2MnBO_5, the decoupled magnetic sub-lattices character of Fe_3BO_5 is preserved : magnetic order on 3LL1 ($\mathbf{k}_1 = (0\ 0\ \frac{1}{2})$, moments along b) survives with reduced magnetic moment, while the correlation length of the magnetic order on 3LL2 ($\mathbf{k}_2 = (0\ 0\ 0)$, moments along a) decreases. In contrast, for x = 1.5, a new $\mathbf{k} = (0\ 0\ 0)$ magnetic ordering, coupling both sub-lattices, is observed, with all moments aligned along c. These results provide new insight on the physical properties of the system, which are discussed in terms of three main parameters : (i) non-linear evolution of the substitution on each sub-lattice, (ii) changes in the direct-exchange and super-exchange couplings as Mn^{2+} ($3d^5$, isoelectronic with Fe^{3+}) is introduced in the structure, and (iii) competing easy-axis anisotropy and magnetic exchanges along the 3LL legs in the decoupled sub-lattice regime. These three parameters are at the origin of an extremely rich (x, T) magnetic phase diagram in the $Fe_{3-x}Mn_xBO_5$ system.

I. INTRODUCTION

Ludwigite oxyborates correspond to the $M_2M'BO_5$ formula (where M and M' are transition metals), as a reference to the mineral Mg_2FeBO_5 [1]. Vonsenite Fe_3BO_5 [2] is one of the most studied ludwigites [3], [4], [5] ; it crystallizes at room temperature in the *Pbam* (# 55) space group (a = 9.462 Å, b = 12.308 Å, and c = 3.075 Å), with four non-equivalent iron sites, Fe1 ($2a$), Fe2 ($2d$), Fe3 ($4g$) and Fe4 ($4h$) (Figure 1a), following a commonly used labeling [6], [7], [8]. Its structure may be viewed as FeO_6 octahedra sharing edges and corners, to build five octahedra long and three octahedra wide zig-zag walls parallel to the c direction (Figure 1a). These walls delimit triangular tunnels, also running along the c axis, occupied by boron atoms in triangular BO_3 coordination (O1, O3 and O5 in Figure 1a). Another structural description is also used in the literature [9], with two types of three-leg ladder (3LL) sub-lattices, consisting of three edge- or corner-sharing octahedra units, or triads, stacked along c : Fe4-Fe2-Fe4 (3LL1) and Fe3-Fe1-Fe3 (3LL2) (Figures 1b and 1c).

Fe_3BO_5 presents interesting physical properties, owing to the mixed valency 2 Fe^{2+} : 1 Fe^{3+}, and the fact that Fe^{3+} species (S = 5/2) occupy 3LL1 sites, while sites 1 and 3 (3LL2) are occupied by Fe^{2+} (S = 2) only [4], [10]. Below 290 K, charge ordering (CO) on 3LL1 leads to a supercell with a doubling of the c parameter, as evidenced by single crystal X-ray and electron diffraction [6], [8], [11]. These unusual features also impact magnetic properties, with two magnetic transitions, corresponding to the independent orderings of 3LL1 (T_{N1} = 112 K) and 3LL2 (T_{N2} = 70 K) [8]. Fe_3BO_5 was also recently shown to exhibit magnetodielectric and multiferroic properties [11], and was also explored as a potential anode for lithium-ion batteries [12]. A number of interesting features can therefore be found in ludwigites : low-dimensional magnetic units, coexistence of paramagnetism and magnetic order, or mixed valency with a non-random distribution of the species on different crystallographic sites. Although the ludwigite structure is able to incorporate various elements, including tetravalent cations, as shown by the long list of known minerals exhibiting this structure (e.g. fredrikssonite [13], bonaccordite [14], azoproite [15], chestermanite [16], etc.), few reports deal with homometallic [17] or heterometallic ludwigites containing Mn, the latter focusing mostly on Cu_2MnBO_5 [18], [19], [20], or $Mn_{3-x}Ni_xBO_5$ [21], [22]. In the only published study of the heterometallic ludwig-

ite system $Fe_{3-x}Mn_xBO_5$, Maignan *et al.* report very distinct *dc* susceptibilities for the x = 0 and x = 1 members, in addition to superparamagnetic-like spin dynamics for x = 1, in spite of the close spin configurations of Mn^{2+} and Fe^{3+}, both being d^5 cations [11]. Moreover, the pyroelectric current measurements performed on these compounds reveal a larger polarization value at 5 K for Fe_2MnBO_5 than for Fe_3BO_5, coupled with the disappearance of CO features, urging for a better understanding of the general impact of Mn substitution on the vonsenite properties, also supported by the known importance of CO and Fe octahedral geometry in explaining the physical properties of Fe_3BO_5 [23]. To this end, an investigation of the $Fe_{3-x}Mn_xBO_5$ system was undertaken. Synchrotron X-ray and neutron diffraction experiments, combined with magnetic susceptibility vs. temperature and X-ray absorption spectroscopy measurements were carried out. A complex magnetic phase diagram emerges, underlining the role of preferred substitution and its impact on the magnetic exchanges and anisotropy, and sublattices coupling.

II. EXPERIMENTAL

$Fe_{3-x}Mn_xBO_5$ ($0 \leq x \leq 3$) samples were prepared by solid state reaction at high temperature. Amounts of precursors were calculated to respect the O_5 stoichiometry. Mixtures of (Fe, Fe_2O_3, MnO and B_2O_3) or (Fe_2O_3, MnO_2, MnO and B_2O_3) were used for $0 \leq x \leq 1.75$ and $2 \leq x \leq 3$, respectively. Powders were pressed in the shape of bars or pellets and heated in evacuated quartz ampoules during 48 hrs at 950°C or 1000°C, respectively. For neutron diffraction experiments, specific samples (x = 0.5, 0.75, 1 and 1.5) were made from ^{11}B enriched B_2O_3.

The quality of the samples was checked by X-ray powder diffraction (XRPD) at room temperature (RT), using a PANalytical diffractometer (using Co or Cu Kα radiations). Small amounts of impurities are difficult to avoid in this system, mainly Fe_3O_4 and $Mn_3B_2O_6$ for smaller and larger x values, respectively. The samples were of poorer quality for $2 \leq x \leq 3$, and their analysis was limited to XRPD measurements only.

Direct current (*dc*) magnetic susceptibility (χ) was derived from magnetization data recorded in a field of 100 Oe, on warming from 5 to 300 K after a zero-field (*zfc*) or field (*fc*) cooling (MPMS, Quantum Design). Alternating current (*ac*) susceptibility was measured in the frequency range 10^1 – 10^4 Hz (h_{dc} = 0 Oe and h_{ac} = 10 Oe) (PPMS, Quantum Design).

X-ray absorption near edge structure (XANES) measurements were performed on the ODE beamline at the SOLEIL synchrotron for the $0.25 \leq x \leq 1.5$ compositions. The X-ray absorption spectra were measured in a transmission configuration and recorded at RT with an energy resolution of 0.5 eV. The spectra were calibrated in energy using Fe and Mn foil references, and normalized using the Larch package [24].

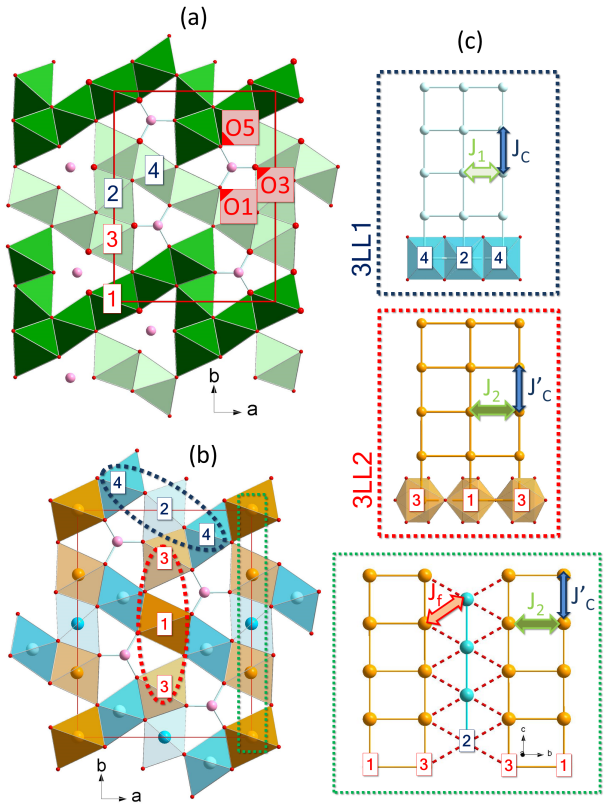

FIG. 1. (color online) : (a) Representation of the vonsenite Fe_3BO_5 structure (projected along the *c* direction), highlighting the FeO_6 octahedra sharing edges and corners to build five octahedra long and three octahedra wide zig-zag walls (dark and light green ribbons). O1, O3 and O5 label oxygens of a triangular BO_3 unit (boron atoms in pink). (b) Same projection of the structure highlighting the two types of three-leg ladders Fe4-Fe2-Fe4 (3LL1, in blue) and Fe3-Fe1-Fe3 (3LL2, in orange). (c) 3LL1 and 3LL2 ladders with corresponding first-neighbor magnetic exchange paths (J_C along the legs, J_1 and J_2 along the 3LL1 and 3LL2 rungs, respectively), and triangular topology of the J_f coupling between 3LL1 and 3LL2.

Samples with x = 0.75, 1 and 1.5 were characterized by synchrotron X-ray powder diffraction (SXRPD) on the CRISTAL beamline at the SOLEIL synchrotron (λ = 0.6694 Å) at RT and on BL04-MSPD at the ALBA synchrotron (λ = 0.4421 Å) in the 80 K to 300 K range. The powders were 20 μm sieved and filled in borosilicate capillaries (Ø 0.5 mm).

Neutron powder diffraction (NPD) vs. temperature was performed on the G4.1 diffractometer (λ = 2.426 Å) from 1.5 to 300 K, at LLB-Orphée, for x = 0.75, 1 and 1.5, and on the Meredit diffractometer (λ = 1.4618 Å), at the Nuclear Physics Institute, in the same temperature range, for x = 0.5, 0.75, 1 and 1.5. Rietveld refinements were performed with the Fullprof program [25]. Symmetry

analysis was carried out using the FullprofSuite software [25] and the Bilbao Crystallographic Server [26], [27].

III. RESULTS

A. Crystal structure study of $Fe_{3-x}Mn_xBO_5$

1. *Evolution of the crystal structure of $Fe_{3-x}Mn_xBO_5$ with x at room temperature*

a. Cell parameters

All samples within the series exhibit the ludwigite crystal structure with *Pbam* space group. This agrees with the electron diffraction study performed at RT for x = 0 and 1, which confirmed the *Pbam* cell with no superstructure [11]. The evolution of the lattice parameters, obtained from Rietveld refinements of the XRPD data for $0 \leq x \leq 3$, is shown in Figure 2. For x = 0, the obtained cell parameters are in good agreement with those previously reported [4]. This is, however, not the case for Mn_3BO_5 (x = 3), for which the published single-crystal data [17] reports smaller cell parameters than for Fe_3BO_5, in contrast with our observation of a volume increase of $\approx 5\%$ from x = 0 to 3. As shown in Figure 2, the cell volume increases with x from x = 0 to 2, and then remains roughly constant. The lattice parameters all increase accordingly with x from x = 0 to 2, above which (x > 2), *c* becomes nearly constant, while *b* increases and *a* decreases. Comparing ionic radii (IR) of di- and tri-valent iron and manganese (IR are given in the inset of Figure 2 [28]), this behavior suggests that manganese is divalent up to x = 2. For x > 2, Mn^{3+} (with similar size to Fe^{3+}) may be present, and could be at the origin of the plateau observed in the evolution of the cell volume as a function of x. This will be further confirmed in the light of the cationic distribution and species on each ladder, in section III A 1 d.

b. Cationic distribution

The analysis of the RT NPD data for x = 0.5, 0.75, 1 and 1.5 allows one to quantify the Fe and Mn distribution on the four cationic sites of the ludwigite structure, owing to the significant difference in the Fe/Mn neutron scattering lengths (0.954 and -0.373 10^{-12} cm, respectively). From the comparison of the refinements performed on different neutron diffraction datasets for a given sample, the site occupancy is estimated to be known with a precision of the order of 5% for the four sites (see Table I). The Fe/Mn ratios determined from the refinements are in good agreement with the nominal compositions. The results are summarized in Figure 3, which represents the evolution of the Mn occupancy (in %) on each site vs. the overall Mn composition. The occupancies of sites 1 and 3 (3LL2) are roughly equal (red full squares and empty circles, respectively), an observation that holds for sites 2 and 4 (3LL1) as well (blue full squares and empty circles, respectively), which means that cationic distribution is nearly homogeneous within each ladder. In contrast, the Mn content in 3LL2 is systematically larger than that in 3LL1. Thus the 3LL2 ladder, which is the one containing only Fe^{2+} for x = 0, is preferentially affected by the Mn substitution, but only to some degree, as Mn also substitutes partially 3LL1 before all 3LL2 sites are filled with Mn. This preferred substitution also implies that the 1Fe : 1Mn threshold occurs for different x values depending on the ladder which is considered : x = 0.9 for 3LL2, and x = 2.1 for 3LL1 (black arrows on Figure 3). Another consequence of the Fe/Mn distribution on the transition metal sites is the presence of diffuse scattering of non-magnetic origin (also called Laue monotonic scattering [29]), centered on Q = 1.15 $Å^{-1}$ on all neutron diffraction patterns, from x = 0.75 to 1.5 (inset of Figure 5b, shown for x = 1).

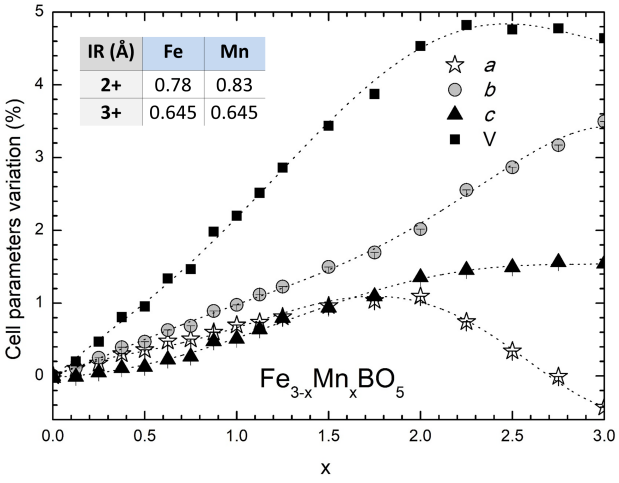

FIG. 2. : Variation (in %) of the lattice parameters *a* (white stars), *b* (grey circles), *c* (black triangles) and cell volume V (black squares) with x in the $Fe_{3-x}Mn_xBO_5$ series (from Rietveld refinements of XRPD data at RT). Cationic sizes of high-spin $Fe^{2+/3+}$ and $Mn^{2+/3+}$ in octahedral environments are given in the inset [28]. Lines are guide to the eye.

c. Fe and Mn valences

Mn K-edge XANES spectra are presented in Figure 4a, along with two reference spectra, MnO (Mn^{2+} species) and Mn_2O_3 (Mn^{3+} species). Similar absorption profiles are observed for all the samples, independently of x, with the white line centred around 6550 eV (lower panel of Figure 4a), likewise to the MnO reference (see upper panel of Figure 4a). Thus, the Mn valence in the $Fe_{3-x}Mn_xBO_5$ series, up to x = 1.5 (highest x value investigated by XANES in this work), is confirmed to be 2+. The amount of Fe^{2+} species decreases with increasing x (Figure 4b), confirming the gradual replacement of Fe^{2+} by Mn^{2+}, which was found to occur preferentially on the 3LL2 ladders (section III A 1 b). Indeed, the comparison with the Fe K-edge XANES reference spectra of FeO (Fe^{2+} species) and Fe_2O_3 (Fe^{3+} species) shows that

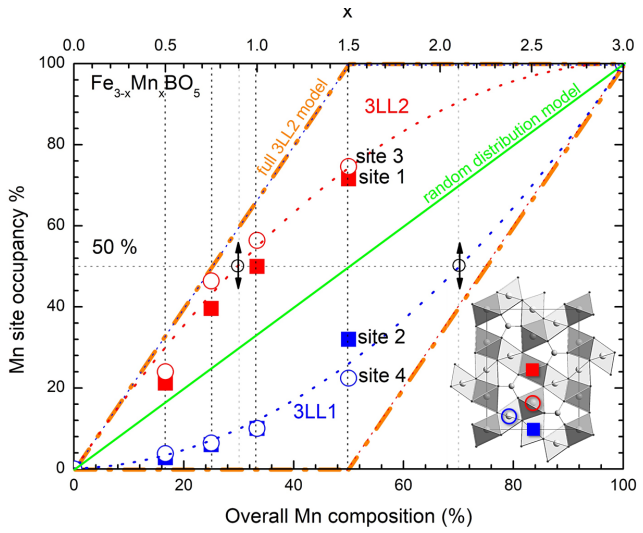

FIG. 3. (color online) : Evolution of the Mn distribution on 3LL1 (sites 2 and 4 drawn as full blue square and empty blue circles) and 3LL2 (sites 1 and 3 drawn as full red square and red blue circles) with x. The green line represents the case of a random distribution of Fe/Mn over both 3LL1 and 3LL2, which thereby become equivalent. The orange dashed line shows the extreme case where Mn is substituted on 3LL2 only, up to an overall composition of 50% of Mn (corresponding to x = 1.5), before gradually substituting 3LL1. The black circles on the horizontal 50% Mn occupancy line correspond to compositions (given by the small arrows) for which the Mn:Fe ratio is 1 in the chosen ladder. Inset : *ab* projection of the ludwigite structure emphasizing the preferred substitution of Mn on the dark grey octahedral sites 1 and 3 of 3LL2.

for x = 0, the absorption edge is close to that of FeO, in good agreement with the expected $2Fe^{2+}$:$1Fe^{3+}$ ratio. Upon Mn-substitution, the Fe absorption edge shifts to higher energies and smoothly meets the Fe_2O_3 absorption edge position at x = 1.5.

d. Evolution of interatomic distances and angles

The evolution of the interatomic distances in $Fe_{3-x}Mn_xBO_5$ was obtained from combined Rietveld refinements using NPD and SXRPD data for x = 1 and 1.5 (Figure 5) and from the literature for x = 0 [8]. The results are summarized in Tables I and II. In Fe_3BO_5, the average <FeO> distance depends on the ladder which is considered : the $Fe2O_6$ and $Fe4O_6$ octahedra forming 3LL1 are the smallest (with <FeO> = 2.09 Å and 2.06 Å, respectively), while iron octahedra in 3LL2 ($Fe1O_6$ and $Fe3O_6$) are bigger (<FeO> = 2.15 Å), in agreement with preferred occupation of Fe^{2+} on 3LL2. A similar observation can be made when increasing x up to x = 1.5, with a slight increase of the <(Fe/Mn)O> distances in all the octahedra, in agreement with the fact that Mn is only present as Mn^{2+} (see sections III A 1 a and III A 1 c). With regards to octahedral distortion, in Fe_3BO_5, $Fe1O_6$ and $Fe2O_6$ (which are in the middle of the triads forming 3LL2 and 3LL1, respectively) are compressed, with one short apical Fe-O distance (x 2) of 2.04 Å and 2.06 Å, respectively, and one (x 4) long distance in the basal plane, of 2.20 Å and 2.11 Å, respectively. The $Fe3O_6$ and $Fe4O_6$ octahedra are more distorted, with three sets of Fe-O distances, ranging between 1.95 Å and 2.21 Å. In all octahedra, the O-Fe-O angles also clearly deviate from 90°.

Comparison with $Fe_{1.5}Mn_{1.5}BO_5$ shows that, although the $(Fe/Mn)2O_6$ octahedron of 3LL1 is more regular than in Fe_3BO_5, there is actually little evolution of octahedral distortions with x (Table II). This particular behavior probably originates from the fact that there is no possible atomic displacement along the *c*-axis (all atoms being on (x y 0) or (x y $\frac{1}{2}$) sites), and that the transition metal octahedra are more flexible than the BO_3 units with their short B-O distances ($\approx$ 1.4 Å). This underlying rigidity of the BO_3 triangles could also be the reason why high levels of Mn substitution (x $\geq$ 2) seem difficult to achieve in the series. It should be underlined further that O4 has a systematically "underbonded" character (short (Fe/Mn)3-O4 and (Fe/Mn)4-O4 distances), which is likely correlated with its specific position, linking both types of ladders and two zig-zag walls, while not being involved in a BO_3 triangle. It leads to a clear displacement of atoms on sites 3 and 4 of the ludwigite structure from the center of their O_6 octahedra.

2. Crystal structure of the $Fe_{3-x}Mn_xBO_5$ series at low temperature

For x = 0.5, 0.75, 1 and 1.5, the *Pbam* crystal structure is observed down to 4 K from high resolution NPD, and further confirmed by SXRPD data at 122 K for x = 1. The lack of charge-ordering (CO) superstructures reported earlier by electron microscopy for x = 1 down to 90 K [11] supports the fact that Mn substitution suppresses charge ordering at least for x $\geq$ 1, but this remains to be confirmed for x = 0.5 and 0.75. For all samples up to x = 1.5, the contraction of the cell parameters with temperature is regular within the experimental error, and similar along *a*, *b*, and *c*. Table III summarizes the results of NPD data Rietveld refinements performed at 180 K and 4 K for x = 1. It shows that there is a general decrease, with decreasing temperature, of the distances between transition metal sites, with the exception of the distance between sites 1 and 3 (d_{1-3}) in 3LL2, and sites 1 and 4 (d_{1-4}), which slightly increases or stays constant within the standard deviation. Similarly, the contraction of the (Fe/Mn) octahedra is only slight, and the octahedral distortion remains almost constant when temperature decreases.

TABLE I: Results of combined SXRPD and NPD Rietveld refinements of Fe_2MnBO_5 and $Fe_{1.5}Mn_{1.5}BO_5$ at 300 K (space group *Pbam*, # 55). (Fe/Mn)1 and (Fe/Mn)2 are on Wyckoff sites 2*a* (0 0 0) and 2*d* ($\frac{1}{2}$ 0 $\frac{1}{2}$) respectively. All other atoms are on sites 4g (x y 0) or 4*h* (x y $\frac{1}{2}$). Cell parameters and atomic positions in Fe_3BO_5 (x = 0) at 320 K (from single-crystal X-ray diffraction data [8]) are given for comparison. Isotropic thermal displacements parameters B were constrained to be identical for a given element. The B values obtained from SXRPD data are (in Å^2) : $B_{Fe/Mn}$ = 0.4(1), B_B = 0.3(1); B_O = 0.3(1) for x = 1, and $B_{Fe/Mn}$ = 0.7(1), B_B = 0.2(1); B_O = 0.8(1) for x = 1.5.

Composition		x = 0 [8]	x = 1	x = 1.5
Cell parameters (Å)	*a*	9.645	9.5223(3)	9.5457(4)
	b	12.310	12.4283(4)	12.4885(5)
	c	3.077	3.0914(1)	3.1037(1)
Cell volume V (Å^3)		365.3	365.9(3)	370.0(2)
Fe/Mn (%)	Site 1	100/0	50(5)/50(5)	28(5)/72(5)
	Site 2	100/0	90(5)/10(5)	68(5)/32(5)
	Site 3	100/0	44(5)/56(5)	25(5)/75(5)
	Site 4	100/0	90(5)/10(5)	78(5)/22(5)
(Fe/Mn)3 (4*g*)	x	0.00029(3)	0.0001(3)	0.0004(9)
	y	0.27433(3)	0.2753(2)	0.2761(6)
(Fe/Mn)4 (4*h*)	x	0.74436(3)	0.7411(3)	0.7389(6)
	y	0.38746(3)	0.3863(2)	0.3851(6)
B (4*h*)	x	0.2687(3)	0.271(2)	0.270(1)
	y	0.3617(2)	0.361(2)	0.362(1)
O1 (4h)	x	0.8431(2)	0.843(1)	0.844(2)
	y	0.0427(1)	0.0432(1)	0.044(1)
O2 (4*g*)	x	0.3874(2)	0.3852(9)	0.386(2)
	y	0.0787(1)	0.0767(9)	0.075(1)
O3 (4*h*)	x	0.6229(2)	0.6256(9)	0.625(1)
	y	0.1382(1)	0.1386(9)	0.139(2)
O4 (4*g*)	x	0.1130(2)	0.1135(9)	0.112(2)
	y	0.1408(1)	0.1410(9)	0.142(2)
O5 (4*h*)	x	0.8409(2)	0.838(1)	0.841(2)
	y	0.2360(1)	0.2361(9)	0.236(1)
SXRPD R_{Bragg} (%)			5.9	5.2
NPD R_{Bragg} (%)			9.2	8.2
χ^2			3.01	3.44

B. Magnetic properties and magnetic structures of $Fe_{3-x}Mn_xBO_5$

Mn for Fe substitution has a strong impact on the magnetic properties of the system. Qualitatively, two types of behaviors are observed depending on x, which are described below. For all compounds, the inverse of the susceptibility curve does not reach a linear regime up to 300 K, which indicates magnetic interactions at high temperature.

1. Magnetic properties and magnetic orderings for x ≤ 1.0

The T_{N1} and T_{N2} values used in the following are derived from susceptibility measurements (Figure 6) and are also listed in Table IV for four selected compositions. The χ(T) curve of Fe_3BO_5 (x = 0, Figure 6a) shows two magnetic transitions, at $T_{N1} \approx 112$ K and $T_{N2} \approx 70$ K, with a strong *zfc*/*fc* effect for T < 70 K, which extends up to T_{N1}. All those features are in good agreement with those published earlier [10], in which T_{N1} and T_{N2} values of 114 K and 74 K, respectively, were reported. These two magnetic transitions correspond perfectly to the independent orderings of the 3LL1 (below 112 K) and 3LL2 (below 70 K) ladders described in [8]. For x = 0.25 and x = 0.5 (Figure 6b and 6c), both transitions are still present, but the kink characterizing T_{N1} is hardly visible (Figure 6f), while the hysteresis below T_{N2} persists. T_{N1} and T_{N2} values are seemingly not affected by Mn substitution in this range of x. The main difference with x = 0 is the fact that the 5 K value of the *fc* susceptibility is negative, with the *fc* susceptibility curve crossing the *zfc* one below a crossing point temperature T_{cross}. This is a well-known feature of magnetic compounds with two magnetic sub-lattices [30] and confirms the fact that small levels of Mn substitution preserve the distinct orderings of 3LL1 and 3LL2 units, a rare observation in heterometallic ludwigites, to the best of our knowledge. For higher x (e.g. x = 0.75, Figure 6d), the peak shape of the *fc* χ(T) below T_{N2} disappears, while the difference between *zfc* and *fc* curves persists. A small kink at T_{N1} is still observed. T_{N1} and T_{N2} are reduced with respect to 0 ≤ x ≤ 0.5 : for x = 0.75, $T_{N1} \approx 100$ K and $T_{N2} \approx 55$ K. Increasing the Mn content further, a drop of the susceptibility maximum, by a factor 10 compared to x = 0, is observed (x = 1, Figure 6e). Two magnetic

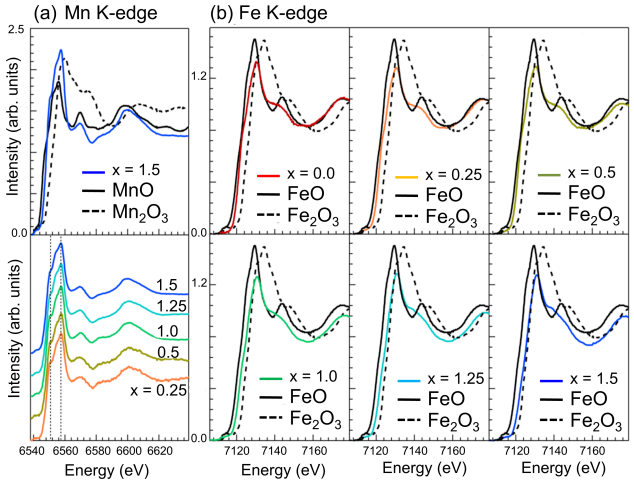

FIG. 4. (color online) : (a) Upper panel: Mn K-edge absorption spectrum of $Fe_{1.5}Mn_{1.5}BO_5$, the measured spectrum is compared to the reference spectra of MnO (black solid lines) and Mn_2O_3 (black dashed lines). Lower panel: Mn K-edge absorption spectra of $Fe_{3-x}Mn_xBO_5$ samples (x = 0.25 to 1.5). The data are shifted vertically for clarity. The two black dashed lines are guide to the eyes to highlight the constant energy position of XANES features for all samples. (b) Fe K-edge absorption spectra of $Fe_{3-x}Mn_xBO_5$ samples (x = 0 to 1.5). The measured spectra are compared to the reference spectra of FeO (black solid lines) and Fe_2O_3 (black dashed lines).

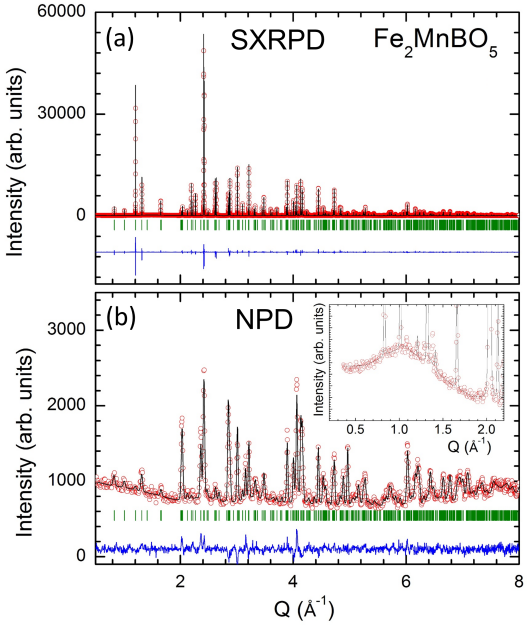

FIG. 5. (color online) : Combined Rietveld refinements of the (a) SXRPD ($\lambda = 0.6694$ Å) and (b) NPD ($\lambda = 1.4618$ Å) data of Fe_2MnBO_5 at 300 K. Inset of (b) : Low Q enlargement of the NPD pattern, to show the diffuse scattering due to Fe/Mn distribution ($\lambda = 2.426$ Å) at 300 K.

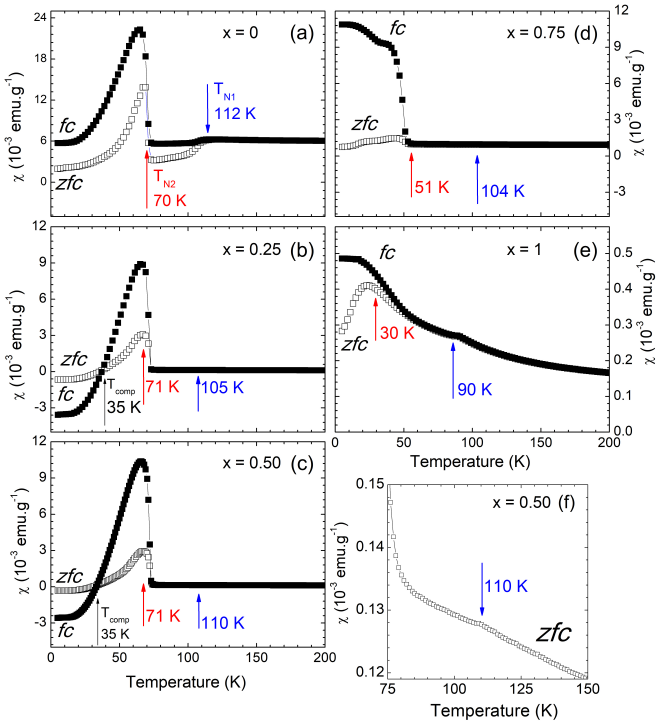

FIG. 6. (color online) : Temperature evolution of the *zfc* and *fc* magnetic susceptibility χ in 100 Oe in the $Fe_{3-x}Mn_xBO_5$ system, for x = 0 (a), 0.25 (b), 0.50 (c), 0.75 (d) and x = 1 (e). (f) shows an enlargement of the χ(T) for x = 0.50 around T_{N1}. Arrows show for each composition T_{N1} (in blue) and T_{N2} (in red).

transitions are still identified, but at lower temperatures with respect to smaller x values (see Table IV). The difference between *zfc* and *fc* curves is also present, like for smaller x values, but starts between T_{N1} and T_{N2}.

TABLE II: Selected atomic distances (in Å) at 300 K (with multiplicity) in Fe_2MnBO_5 and $Fe_{1.5}Mn_{1.5}BO_5$ at 300 K. For simplicity, the distance between (Fe/Mn) sites is written using only the site number, e.g. the distance between (Fe/Mn)1 and (Fe/Mn)3 is noted d_{1-3}. Atomic distances in Fe_3BO_5 (x = 0) at 320 K (calculated from [8]) are given for comparison purposes.

Composition	x = 0	x = 1	x = 1.5
(Fe/Mn)1-O	2.2020 x4	2.212(3) x4	2.216(5) x4
	2.0367 x2	2.060(4) x2	2.072(7) x2
<(Fe/Mn)1-O>	2.147	2.161(4)	2.168(7)
(Fe/Mn)2-O	2.1075 x4	2.119(2) x4	2.115(4) x4
	2.0609 x2	2.098(3) x2	2.104(7) x2
<(Fe/Mn)2-O>	2.092	2.112(3)	2.111(7)
(Fe/Mn)3-O	2.2058 x2	2.228(2) x2	2.226(5) x2
	2.2075 x2	2.234(3) x2	2.225(5) x2
	1.9596	1.987(4)	1.980(7)
	2.1012	2.139(4)	2.151(7)
<(Fe/Mn)3-O>	2.148	2.175(4)	2.181(7)
(Fe/Mn)4-O	2.0913 x2	2.118(2) x2	2.151(5) x2
	2.0084 x2	1.996(2) x2	2.001(4) x2
	2.0826	2.112(4)	2.143(7)
	2.0763	2.085(4)	2.100(7)
<(Fe/Mn)4-O>	2.058	2.072(4)	2.091(7)
d_{1-3}	3.378	3.422(2)	3.448(6)
d_{2-4}	2.788	2.841(3)	2.875(6)
d_{2-3}	3.176	3.191(2)	3.197(6)
d_{1-4}	3.104	3.107(2)	3.110(6)
d_{3-4}	3.190	3.224(3)	3.238(9)

To go further in the understanding of these complex magnetic behaviors, neutron diffraction vs. temperature was performed for x = 0.75 and x = 1. Similar behaviors are observed for both compounds. Below T_{N1}, additional peaks appear on the NPD patterns (x = 1, Figure 7), which can be indexed by the commensurate propagation vector $\mathbf{k}_1 = (0\ 0\ \frac{1}{2})$, as in the model proposed for Fe_3BO_5 [8]. Rietveld refinements supported by symmetry analysis (Table V) indicate that only the 3LL1 sub-lattice orders below T_{N1}. As there is no evidence of a structural transition in Mn substituted samples, a simple *Pbam* cell was considered for the symmetry analysis. Magnetic ordering of symmetry nonequivalent sites 2 and 4 (which form 3LL1) follows the irreducible representation (irrep) Γ6, with two basis vectors $\psi 1 = (1\ 0\ 0)$ and $\psi 2 = (0\ 1\ 0)$. Interestingly, for the Γ6 irrep, magnetic ordering is also allowed on sites 1 and 3 (3LL2), but only with moments parallel to *c*, which is not compatible with the observed magnetic intensities. The best refinement results therefore correspond to a magnetic ordering, below T_{N1}, on the 3LL1 sub-lattice only, and can be described as FM ladder rungs, arranged AFM along *c*, with spins parallel to *b* (Figure 7b). The magnetic space group is then P_bnma (BNS #62.451) in a cell doubled along *c*. This group is not compatible with ferroelectricity or any magnetoelectric effect [26]. The moments on site 2 and site 4 are not equivalent symmetry-wise and can be refined independently : for x = 1 at 2 K, values of 3 μ_B and 2.2 μ_B are obtained on site 2 and 4, respectively (Table IV and Figure 7e). This is only slightly lower than the values reported for Fe_3BO_5 [8] (3.9 μ_B and 2.7 μ_B at 10 K, respectively, which were already distinctively smaller than the 5 μ_B and 4 μ_B expected for spin-only values of Fe^{3+} and Fe^{2+}), but the tendency to have a larger moment on site 2 (which has the least distorted octahedral environment) than on site 4 is confirmed for both x = 0.75 and x = 1 (Table IV). These moments values, close to those observed for x = 0, are also in good agreement with the fact that 3LL1 is little impacted by Mn substitution up to x = 1 (Figure 3).

Below T_{N2}, the ordering of the second sub-lattice leads to additional magnetic intensity (x = 1, Figures 7a and 7d) on existing Bragg peaks ($\mathbf{k}_2 = (0\ 0\ 0)$), likewise to Fe_3BO_5 [8]. For x = 0.75, the corresponding magnetic Bragg peaks are only slightly broader than the crystal ones (whose width is limited by instrumental resolution), whereas for x = 1, broad magnetic scattering is observed, as highlighted on the inset of Figure 7a for the (0 2 0) Bragg peak. Rietveld refinements, performed using symmetry analysis, indicate that the magnetic ordering of this 3LL2 sub-lattice follows irrep Γ5, that is, AFM configuration within the rungs, with a FM arrangement along *c* (Figure 7c). Moments are aligned along *a*, therefore inferring a magnetic anisotropy on 3LL2, like on 3LL1, of the easy-axis type, but orthogonal to the latter. For x = 0.75 at 2 K, the ordered moment values on sites 1 and 3 are 2.9 μ_B and 2.8 μ_B, respectively. For x = 1, the ordering is only short-range, with a magnetic correlation length estimated about 120 Å, and the maximal ordered moment remains low, around 1.6 μ_B (Figure 7e). This value was constrained to be equal for both sites 1 and 3, since the refinement did not allow for a meaningful distinction between the two. This short-range magnetic ordering is in good agreement with the preferred substitu-

TABLE III. Selected atomic distances (in Å) at 180 K and 4 K in Fe_2MnBO_5 (from Rietveld refinement results in the *Pbam* space group using high resolution NPD data).

	180 K	4 K
Cell parameters (Å)		
a	9.5147(3)	9.5064(3)
b	12.4146(4)	12.4065(4)
c	3.0870(1)	3.0845(1)
Cell volume V (Å^3)	364.6(2)	363.8(2)
(Fe/Mn)1-O	2.218(8) x4	2.202(9) x4
	2.03(1) x2	2.02(1) x2
<(Fe/Mn)1-O>	2.16(1)	2.14(1)
(Fe/Mn)2-O	2.110(6) x4	2.095(7) x4
	2.08(1) x2	2.09(1) x2
<(Fe/Mn)2-O>	2.10(1)	2.09(1)
(Fe/Mn)3-O	2.23(1) x2	2.24(2) x2
	2.21(2) x2	2.18(2) x2
	2.06(2)	2.03(2)
	2.10(2)	2.12(2)
<(Fe/Mn)3-O>	2.17(2)	2.16(2)
(Fe/Mn)4-O	1.993(7) x2	2.001(7) x2
	2.113(8) x2	2.118(8) x2
	2.06(1)	2.07(1)
	2.12(1)	2.12(1)
<(Fe/Mn)4-O>	2.06(1)	2.07(1)
d_{1-3}	3.44(2)	3.47(2)
d_{2-4}	2.824(7)	2.814(7)
d_{2-3}	3.17(1)	3.14(1)
d_{1-4}	3.114(6)	3.122(6)
d_{3-4}	3.17(2)	3.09(2)

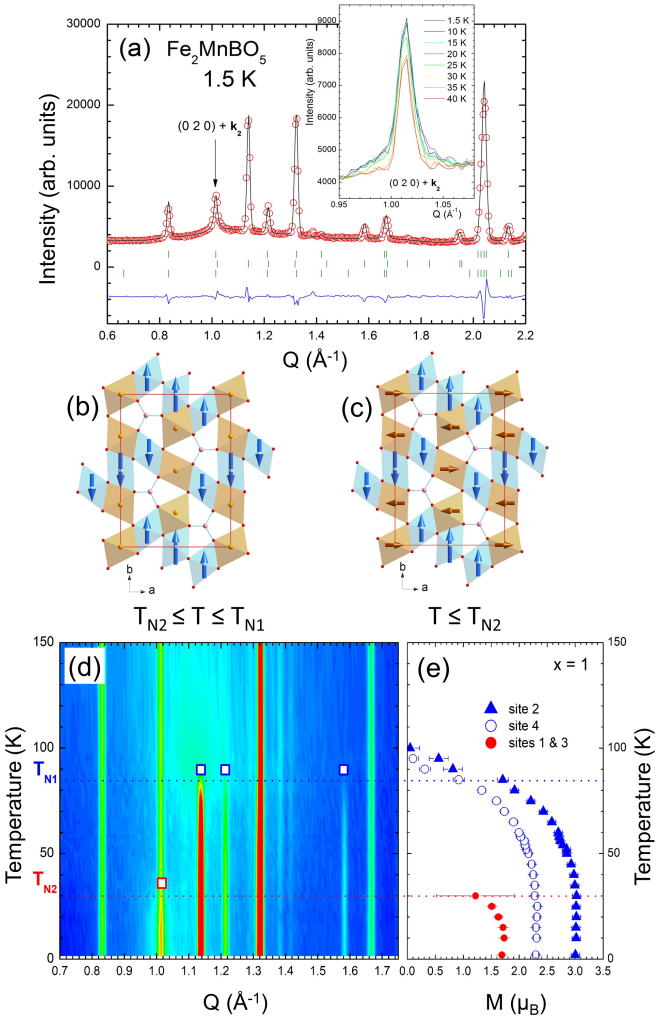

FIG. 7. (color online) : (a) Rietveld refinement of the NPD data for x = 1 at 1.5 K. Inset : enlargement of the (0 2 0) peak to illustrate additional magnetic intensity below 35 K. Right panel : Magnetic ordering on 3LL1 (blue) and 3LL2 (orange) depending on the temperature range considered ($T_{N2} \leq T \leq T_{N1}$ (b) and $T \leq T_{N2}$ (c)). (d) Temperature evolution of the NPD patterns of Fe_2MnBO_5 (left) and corresponding evolution of the refined magnetic moment on each (Fe/Mn) site (e). Blue (red) empty squares indicate the main magnetic Bragg peaks observed below T_{N1} (T_{N2}) in (d).

tion of Mn^{2+} on 3LL2, which leads to a Fe:Mn ratio close to 1 on 3LL2 for x = 1. At 2 K, the magnetic space group of the cell is therefore lowered to *Pb'am'* (BNS #55.358), whose point group is not compatible with ferroelectric or magnetoelectric effects, although the Mn for Fe substitution could actually lower the symmetry locally. Two representations are thus mixed below T_{N2} ($\Gamma 6 \oplus \Gamma 5$), which means that the magnetic phase transition at T_{N2} is first-order, while the transition at T_{N1} is second-order. This should also apply to Fe_3BO_5, and is in good agreement with specific heat data [31].

For both x = 0.75 and x = 1, signatures of magnetic disorder are also seen on the *ac* susceptibility curves (Figure 8), which becomes frequency dependent below 30 K for both compositions. As a final remark, in contrast to what was reported for Fe_3BO_5 [8], the ordering of 3LL2 does not seem to influence the 3LL1 ordered moment value.

2. *Magnetic properties and magnetic ordering for 1.0 ≤ x < 2.0*

For larger x values ($1 < x < 2$) the χ(T) curves still display two transitions, as shown in Figure 9a for x = 1.5, corresponding to the splitting of the *zfc* and *fc* curves at $T_N \approx 100$ K, and to the downturn of the *zfc* curves at $T_{down} \approx 30$ K. Neutron diffraction performed on $Fe_{1.5}Mn_{1.5}BO_5$ shows a unique transition at $T_N = 100$ K, corresponding to the appearance of magnetic intensity, with the propagation vector $\mathbf{k} = (0\ 0\ 0)$. Rietveld refinements (Figure 10) based on symmetry analysis indicate that the magnetic order follows one single representation, $\Gamma 1$, for the four different sites. This imposes moments along *c*, and the magnetic space group is therefore *Pbam* (BNS #55.353, not compatible with ferroelectric or direct magnetoelectric effects). For sites 1 and 2, this couples the components of (x, y, z) and (-x+$\frac{1}{2}$, y+$\frac{1}{2}$, -z) AFM along *c*. For sites 3 and 4, the coupling within (x,

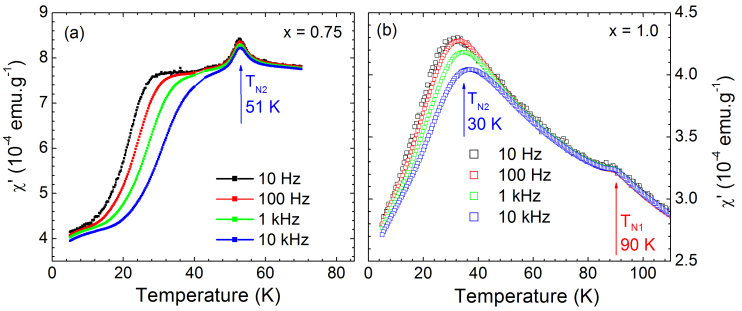

FIG. 8. (color online) : *ac* susceptibility measurements vs. temperature as a function of frequency f (10 Hz to 10^4 Hz) for x = 0.75 and x = 1 in the $Fe_{3-x}Mn_xBO_5$ system (in 10 Oe).

y, z) and (-x, -y, z), as well as (-x+$\frac{1}{2}$, y+$\frac{1}{2}$, -z) and (x+$\frac{1}{2}$, -y+$\frac{1}{2}$, -z) pairs is FM, and the pairs are coupled together antiferromagnetically (Figure 10a). The comparison of Figure 7c and 10a (also summarized in Figure 11) shows how most couplings have been reversed, especially within the triads of former 3LL subunits.

There is no symmetry constraint between the moment values on each sites and the refinement is improved significantly by refining them independently. While the moments on sites 2 and 4 are almost identical, 2.7 μ_B, there is a significantly lower magnetic moment on site 1 (1.7 μ_B), with respect to site 3 (2.5 μ_B), despite similar Fe/Mn ratios (Table IV). In addition, the magnetic peaks are resolution limited, in contrast to x = 0.75 and x = 1, but a frequency dependence of the *ac* susceptibility curves (inset of Figure 9a) is still observed around 30 K, like for x = 0.75 and x = 1. It does not seem to be linked with any feature on the NPD patterns, except for a slight decrease of the observed ordered moment on all sites (Figure 9b), which coincides with the decrease in the *zfc* magnetization curve (Figure 9a) below 30 K.

3. *$Fe_{3-x}Mn_xBO_5$ magnetic phase diagram*

From the susceptibility curves, such as those shown in Figures 6 and 9, a (x, T) magnetic phase diagram was built, and is displayed in Figure 11. T_{N1} (blue squares) and T_{N2} (red squares), corresponding to the ordering of 3LL1 and 3LL2, respectively, are plotted up to x = 1. T_{N2} corresponds to the maximum of the peak of the *zfc* susceptibility curve up to x = 1, which is also in agreement with the T_{N2} determined from NPD data. For x > 1, T_N is defined as the temperature where *zfc* and *fc* χ curves split markedly. In the phase diagram are also reported T_{cross} (crossing point temperature of the *zfc* and *fc* curves, white up triangles) and T_{down}, which corresponds for x > 1 to the temperature of the maximum on the *zfc* susceptibility curve (white down triangles). The temperature at which *ac* frequency effects are observed

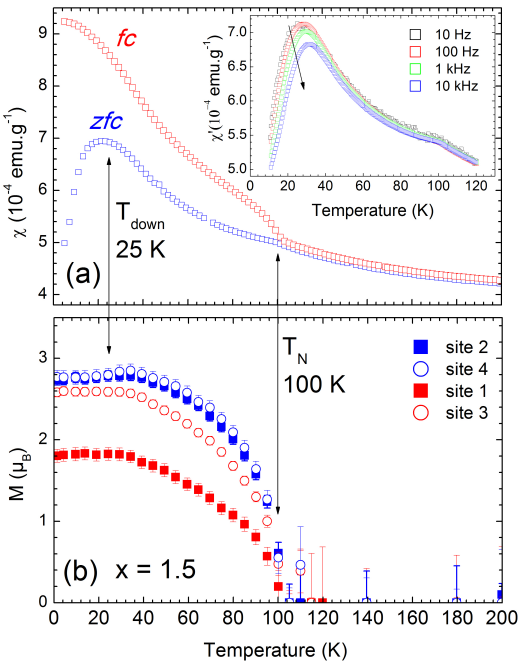

FIG. 9. (color online) : (a) Magnetic susceptibility (*zfc* and *fc*) measurements for x = 1.5 in 100 Oe ; the inset shows corresponding *ac* susceptibility measurements in the range 10 Hz-10^4 Hz in 10 Oe. (b) Temperature evolution of the ordered magnetic moment on each site for $Fe_{1.5}Mn_{1.5}BO_5$ (from NPD data). T_N and T_{down} are shown by black arrows.

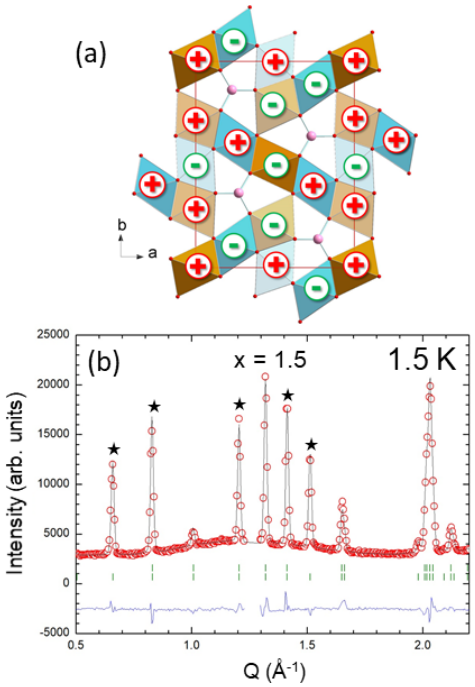

FIG. 10. (color online) : (a) Illustration of the magnetic ordering for x = 1.5 and (b) corresponding NPD data Rietveld refinement at 1.5 K. Stars indicate the main magnetic Bragg peaks. In (a) the moments are along *c* and symbolised by + or – signs depending on their direction.

TABLE IV. Evolution of T_N with x (from susceptibility measurements and [8] for x = 0), and of the ordered moment on each transition metal site (from Rietveld refinement of NPD data) in the $Fe_{3-x}Mn_xBO_5$ series. The ordered moments for x = 0 were measured at 10 K and are taken from reference [8], while the values for the other compositions were obtained at 2 K.

		x = 0	x = 0.75	x = 1.0	x = 1.5
		T_{N1} = 112 K T_{N2} = 70 K	T_{N1} = 104 K T_{N2} = 51 K	T_{N1} = 90 K T_{N2} = 30 K	T_N = 100 K
3LL1	Site 2	$M_y = 3.9(1)\ \mu_B$	$M_y = 3.6(1)\ \mu_B$	$M_y = 3.0(1)\ \mu_B$	$M_z = 2.7(1)\ \mu_B$
	Site 4	$M_y = 2.74(7)\ \mu_B$	$M_y = 2.9(1)\ \mu_B$	$M_y = 2.2(1)\ \mu_B$	$M_z = 2.7(1)\ \mu_B$
3LL2	Site 1	$M_x = 3.3(2)\ \mu_B$	$M_x = 2.9(2)\ \mu_B$	$M_x = 1.6(4)\ \mu_B$	$M_z = 1.7(1)\ \mu_B$
	Site 3	$M_x = 4.0(1)\ \mu_B$	$M_x = 2.8(2)\ \mu_B$	$M_x = 1.6(4)\ \mu_B$	$M_z = 2.5(1)\ \mu_B$

on susceptibility curves is also shown in Figure 11 (white stars).

The main feature of the phase diagram is the existence of two main types of magnetic orders, with a boundary between x = 1 and x = 1.5, characterized by the existence of either two independent magnetic sub-lattices (x $\leq$ 1) or by a single magnetic network (1 < x $\leq$ 1.75). Up to x = 0.5, there is little change with x of the magnetic ordering temperatures, which remain roughly constant $\approx$ 110 K and 70 K, before a sharp decrease is observed for x $\geq$ 0.75. A decrease of the ordered magnetic moment (Table IV) and the appearance of frequency effects on the *ac* susceptibility below 30 K are also observed for x $\geq$ 0.75, likely owing to magnetic disorder. Based on this phase diagram, x $\approx$ 1.25 should correspond to the absence of ordering on 3LL2, while T_{N1} should be reduced to $\approx$ 70 K. Further increasing x (x $\geq$ 1.5), one reaches the single magnetic lattice regime, with T_N increasing from 100 K, for x = 1.5, up to 115 K for x = 1.75. Low temperature *ac* susceptibility frequency effects are still observed up x = 1.5, but could be expected to decrease with increasing Mn content, as T_N increases and magnetic disorder vanishes.

This experimental study proves the originality of the magnetic properties of the $Fe_{3-x}Mn_xBO_5$ ludwigite borates, coming from an unusual crystal structure, with the addition of preferred Fe/Mn distribution. The different properties which can be impacted when varying x in $Fe_{3-x}Mn_xBO_5$ are now discussed in more details below.

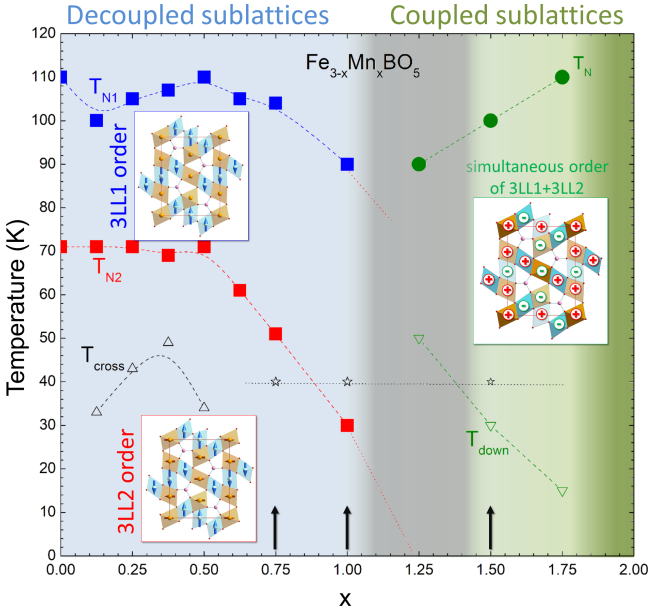

FIG. 11. (color online) : (x, T) phase diagram of the $Fe_{3-x}Mn_xBO_5$ system. T_{N1} and T_{N2} (x $\leq$1) or T_N (x > 1) are shown as blue squares, red squares, and green circles, respectively. T_{cross} and T_{down} are also shown as white triangles pointing up or down, respectively. White stars indicate the onset of *ac* frequency effects in the susceptibility curves. Arrows indicate x values for which neutron diffraction experiments have been performed. The composition range can be separated into decoupled and coupled magnetic sub-lattices, as highlighted by the blue and green areas, respectively. The grey area shows the x range in which the nature of the magnetic ordering changes. The dark green area remains unexplored. Corresponding magnetic orders are illustrated (see also text).

IV. DISCUSSION

a. Charge ordering

From [11], it is known that there is no CO in Fe_2MnBO_5, in contrast with Fe_3BO_5, a result that can be linked with previous reports on other CO systems [32], in which even minute amounts of substitution destroy any ordering of the charges. In Fe_3BO_5, the schematic picture of charge ordering concerns 3LL1 only : the extra electron on each triad of 3LL1 (which contains $2Fe^{3+}$ for $1Fe^{2+}$) is delocalised at high temperature, and then localizes onto a Fe-Fe pair, to form a dimer. The ordering of the dimers along the ladder is zig-zag like, probably as a mean to minimize structural distortions [8]. In $Fe_{3-x}Mn_xBO_5$, because of the preferred substitution of Mn^{2+} on 3LL2, CO could have been expected to withstand sizeable levels of substitutions ; 10% of Mn on 3LL1, as evaluated in Fe_2MnBO_5, is high enough to destroy CO features at least down to 90 K, however. Interestingly, in spite of the absence of CO on 3LL1, the 3LL1 triad remains ferromagnetic up to x = 1, showing

TABLE V. Basis functions for axial vectors associated with irreducible representation Γ6 for Wyckoff site $2d$ (site 2) and $4h$ (site 4) of the *Pbam* space group, with the propagation vector k_1 = (0 0 0.5).

Γ6	(x y z)	(-x+$\frac{1}{2}$ y+$\frac{1}{2}$ -z+1)	(x y z)	(-x+1 -y+1 z)	(-x+$\frac{3}{2}$ y+$\frac{1}{2}$ -z+1)	(x-$\frac{1}{2}$ -y+$\frac{1}{2}$ -z+1)
ψ1	1 0 0	1 0 0	1 0 0	1 0 0	1 0 0	1 0 0
ψ2	0 1 0	0 $\bar{1}$ 0	0 1 0	0 1 0	0 $\bar{1}$ 0	0 $\bar{1}$ 0

that CO dimers do not control the magnetic structure, as it had been suggested in [33], and that their existence has probably less impact on the magnetic ordering than the presence of Fe^{3+} on 3LL1 only. This promises to be a very interesting theoretical issue to investigate. In a similar fashion, based on the importance of octahedral distortions in vonsenite [23], [34], [35], the origin of the preferred substitution, as well as the impact of Mn^{2+} on the magnetism of the 3LL2 units, would also be key points to study theoretically.

b. Understanding magnetic exchanges

A preliminary step is to check whether the changes induced by Mn^{2+} can be explained by the Goodenough-Kanamori rules [36] going from x = 0 to x = 1.5. In Fe_3BO_5, the FM triad (of edge-sharing octahedra) in 3LL1 is simply explained by a d^5-d^6 ferromagnetic direct-exchange (with short Fe2-Fe4 distances ≈ 2.78 Å), J_1 (Figure 1c). Along *c*, FeO_6 octahedra are also linked by edges but the Fe-Fe distance is larger (≈ 3.08 Å), thus close to the limit for a direct-exchange mediated J_C. With a Fe-O-Fe angle of about 94°, a weak d^5-d^6 super-exchange J_C would actually support the observed AF configuration. The coupling between 3LL1 units is mediated by more complex paths, involving super-super exchange, possibly through BO_3 units, which cannot be decided unequivocally at that stage, considering the crystal structure. Within 3LL2 units, as d^6-d^6 interactions only are present, the strongest interactions should correspond to AFM super-exchange J_2 within the triad (octahedra sharing corner), and to ferromagnetic direct-exchange along *c*, corresponding to J'_C (Figure 1c). The Fe-Fe distance along *c* is the same as 3LL1 (≈ 3.08 Å), but the Fe-O-Fe angle is actually less distorted, > 90° in 3LL1 for < 90° in 3LL2, which explains why d^5-d^6 interactions are of different signs depending on the ladder, and hence the distinction between J_C and J'_C. The coupling between 3LL1 and 3LL2 units has a triangular topology. The corresponding exchange path J_f (Figure 1c) is through larger Fe-Fe distances (≈ 3.17 Å) between edge-sharing octahedra, and presumably leads to a weaker super-exchange interaction than within a sub-lattice unit. In the $Fe_{3-x}Mn_xBO_5$ system, it is necessary to consider Mn^{2+}, isoelectronic to Fe^{3+} (d^5) in addition to Fe^{3+} and Fe^{2+}. Adding Mn^{2+} to 3LL2 should lead to similar characteristics to those of 3LL1 along *c* in Fe_3BO_5, that is, antiferromagnetic J'_C. The exchange along *c* in 3LL1 and 3LL2 is ferromagnetic, however, as exemplified in x = 1.5. The fact that, in x = 1.5, FM J_C and FM J'_C is observed, rather supports the idea that, in the decoupled sub-lattice regime, antiferromagnetic J_C in 3LL1 is weak, and likely lies at the threshold between AFM super-exchange and FM (d^5-d^6) direct-exchange.

c. Magnetic sub-lattices coupling

The coupling of both ladders for x = 1.5 is concomitant with the observation of ferromagnetic J_C and J'_C exchange along *c* for both 3LLs. Arguably, it can be proposed that, for x ≤ 1, the antiferromagnetic ordering along *c*, of the 3LL1 spins at T_{N1}, prevents the ordering of 3LL2, as the triangular pathways coupling the ladders through J_f frustrate the J'_C magnetic exchange (whether FM or AFM) [5]. Assuming a strong easy-axis magnetic anisotropy of Fe^{2+} [37] [38], the 3LL2 spins cannot order into a non-collinear structure (such as the 120° magnetic ground state observed in frustrated compounds with triangular ladder topology [39], [40]), and remain idle down to T_{N2}. 3LL2 spins eventually order at $T_{N2} << T_{N1}$, perpendicularly to the 3LL1 spins : the release of the frustration is here performed through a magnetic decoupling of both lattices. Although unusual, idle spin behavior linked with topological frustration has been reported in other mixed valence systems, like $Fe^{2+}Fe_2^{3+}F_8(H_2O)_2$ [41], [42]. This coexistence of three-dimensional (3D) order and frustration remains the main feature of the magnetic ordering of the system $Fe_{3-x}Mn_xBO_5$ up to x = 1. Other examples of ladders' coupling in the ludwigite system are scarce or difficult to assess, as there are very few published neutron diffraction studies, which mostly concentrate on Fe_3BO_5 ([8],[5]), and the interpretation of magnetization data is not straightforward, as exemplified by this study. From a literature survey, decoupled ladders could be expected in Co_2FeBO_5, or Ni_2FeBO_5 [43], [44], whereas coupled ladders would be likely in Co_3BO_5 [45] and $Co_{2.5}Sn_{0.5}BO_5$ [46], but this would have to be confirmed by appropriate experiments.

d. Magnetic disorder

The ludwigite system also offers a very interesting approach to study magnetic disorder : preferred substitution can be seen as an additional degree of freedom to adjust the composition of each ladder, concentrating disorder effects on one sub-lattice at a time. Up to x = 1.5, which represents 50% Mn in the system, 3LL1 remains

ordered, with a T_N varying between 112 K (x = 0) and 85 K (x = 1), increasing again to 100 K for x = 1.5. For x $\leq$ 1, the ordering of 3LL1 occurs through super-exchange pathways that are not sensitive to the magnetic state of 3LL2 (i.e., disordered or ordered), and it could be possible by adjusting x to achieve complete disorder on 3LL2, while preserving order on 3LL1, with potentially interesting applications, such as magnetocaloric effects. A more detailed investigation of the composition range 1 < x < 1.5, which lies at the threshold between two distinct magnetic ground states, will also be an interesting perspective, with unusual effects being expected, such as non collinear magnetic ordering resulting from competing anisotropies or exchange disorder. In this context, substitution of 4+ species should also be of interest, since 4+ species might preferentially substitute on 3LL1 rather than on 3LL2, and arguably prevent magnetic ordering altogether, a scenario that can be proposed to explain the spin-glass state of $Co_{2.5}Ti_{0.5}BO_5$ [47]. An inelastic neutron scattering study of the $Fe_{3-x}Mn_xBO_5$ system is now required to provide a better picture of the dominant magnetic exchange paths in the ludwigite structure, in particular to confirm the different hypothesis about the impact of Mn substitution on magnetic exchanges, magnetic anisotropy and on the sub-lattice coupling.

V. CONCLUSION

This detailed study of the crystal and magnetic structures, and magnetic properties of the heterometallic ludwigite system $Fe_{3-x}Mn_xBO_5$, has established a rich phase diagram, originating from its complex network of two crystallographically distinct three-leg ladders. The composition (x) controls both the $(Fe/Mn)O_6$ octahedral distortions and orbital filling. For small x values (x $\leq$ 1), the ladders are decoupled and order independently. A reversal of the magnetic exchange signs inside the different triads is observed above a threshold of x $\approx$ 1.25. In parallel, magnetic exchange along all ladders' legs becomes ferromagnetic, which removes the frustration at the origin of the decoupling of the ladders and leads to a single magnetic transition. Magnetic anisotropy also changes from easy-axis along *a* or *b* for x < 1.25, to easy-axis along *c* for x $\geq$ 1.5. Magnetic relaxation phenomena below 30 K and reduced ordered magnetic moments on the transition metal sites both attest to magnetic disorder, for 0.75 $\leq$ x $\leq$ 1.5. The ability to substitute Mn preferentially on only one of the two ladders is an original way to control both magnetic disorder and ladders' magnetic coupling in this system.

The authors thank S. Dufourd and F. Veillon (CRISMAT) for technical support. This work was supported by the French-Romanian project ANR-UEFISCDI, contracts No. RO-FR/01.01.2013, code PN-II-ID-JRP-2011-2-0056/ANR-12-IS08-0003, COFeIn and the Agence Nationale de la Recherche (ANR-16-CE08-0007-01 contract BORA-BORA). Neutron measurement were performed also at the CANAM infrastructure of the NPI CAS Rez and reactor LVR15 supported through MSMT project No. LM2015056 and LM2015074.

[1] Y. Takeuchi, T. Watanabe, and T. Ito, Acta Crystallographica **3**, 98 (1950).
[2] Y. Takeuchi, Mineralogical Jouranl **2**, 19 (1956).
[3] E. F. Bertaut, Acta Crystallographica **3**, 473 (1950).
[4] H. Steinfink and J. S. Swinnea, American Mineralogist **68**, 827 (1983).
[5] J. P. Attfield, J. F. Clarke, and D. A. Perkins, Physica B **180**, 581 (1992).
[6] M. Mir, R. B. Guimaraes, J. C. Fernandes, M. A. Continentino, A. C. Doriguetto, Y. P. Mascarenhas, J. Ellena, E. E. Castellano, R. S. Freitas, and L. Ghivelder, Physical Review Letters **87**, 147201 (2001).
[7] M. Mir, J. Janczak, and Y. P. Mascarenhas, Journal of Applied Crystallography **39**, 42 (2006).
[8] P. Bordet and E. Suard, Physical Review B **79**, 144408 (2009).
[9] R. B. Guimaraes, M. Mir, J. C. Fernandes, M. A. Continentino, H. A. Borges, G. Cernicchiaro, M. B. Fontes, D. R. S. Candela, and E. Baggio-Saitovitch, Physical Review B **60**, 6617 (1999).
[10] A. P. Douvalis, A. Moukarika, T. Bakas, G. Kallias, and V. Papaefthymiou, Journal of Physics: Condensed Matter **14**, PII S0953 (2002).
[11] A. Maignan, F. Laine, A. Guesdon, S. Malo, F. Damay, and C. Martin, Journal of Solid State Chemistry **246**, 209 (2017).
[12] J. Sottmann, L. Nataf, L. Chaix, V. Pralong, and C. Martin, Journal of Physical Chemistry C **122**, 17042 (2018).
[13] P. J. Dunn, D. R. Peacor, W. B. Simmons, and D. Newbury, Geologiska Foreningen i Stockholm Forhandlingar **105**, 335 (1983).
[14] S. De Waal, E. Viljoen, and L. Calk, South African Journal of Geology **77**, 375 (1974).
[15] A. Konev, V. Lebedeva, A. Kashayev, and Z. Ushchapovskaya, International Geology Review **13**, 1183 (1971).
[16] E. Foord and R. Erd, Canadian Mineralogist **26**, 911 (1988).
[17] A. Utzolino and K. Bluhm, Zeitschrift Fur Naturforschung Section B-a Journal of Chemical Sciences **51**, 1433 (1996).
[18] S. Sofronova, E. Moshkina, I. Nazarenko, Y. Seryotkin, S. A. Nepijko, V. Ksenofontov, K. Medjanik, A. Veligzhanin, and L. Bezmaternykh, Journal of Magnetism and Magnetic Materials **420**, 309 (2016).
[19] E. Moshkina, C. Ritter, E. Eremin, S. Sofronova, A. Kartashev, A. Dubrovskiy, and L. Bezmaternykh, Journal of Physics-condensed Matter **29**, 245801 (2017).
[20] E. M. Moshkina, M. S. Platunov, Y. V. Seryotkin, A. F. Bovina, E. V. Eremin, S. N. Sofronova, and L. N. Bezmaternykh, Journal of Magnetism and Magnetic Materials **464**, 1 (2018).

[21] L. Bezmaternykh, E. Kolesnikova, E. Eremin, S. Sofronova, N. Volkov, and M. Molokeev, Journal of Magnetism and Magnetic Materials **364**, 55 (2014), cited By 12.

[22] E. Moshkina, S. Sofronova, A. Veligzhanin, M. Molokeev, I. Nazarenko, E. Eremin, and L. Bezmaternykh, Journal of Magnetism and Magnetic Materials **402**, 69 (2016).

[23] M. Matos, J. Terra, D. E. Ellis, and A. S. Pimentel, Journal of Magnetism and Magnetic Materials **374**, 148 (2015).

[24] M. Newville, Journal of Physics: Conference Series **430**, 012007 (2013).

[25] J. Rodriguez-Carvajal, Physica B **192**, 55 (1993).

[26] E. Kroumova, M. I. Aroyo, J. M. Perez-Mato, A. Kirov, C. Capillas, S. Ivantchev, and H. Wondratschek, Phase Transitions **76**, 155 (2003).

[27] M. I. Aroyo, A. Kirov, C. Capillas, J. M. Perez-Mato, and H. Wondratschek, Acta Crystallographica Section A **62**, 115 (2006).

[28] R. D. Shannon, Acta Crystallographica Section A **32**, 751 (1976).

[29] B. Warren, X ray diffraction, (Addison-Wesley, 1969) p. 229.

[30] J. S. Smart, American Journal of Physics **23**, 356 (1955).

[31] J. C. Fernandes, R. B. Guimaraes, M. A. Continentino, L. Ghivelder, and R. S. Freitas, Physical Review B **61**, R850 (2000).

[32] A. P. Ramirez, Journal of Physics-condensed Matter **9**, 8171 (1997).

[33] E. Vallejo and M. Avignon, Journal of Magnetism and Magnetic Materials **310**, 1130 (2007).

[34] M. Matos, Journal of Solid State Chemistry **177**, 4605 (2004).

[35] M. H. Whangbo, H. J. Koo, J. Dumas, and M. A. Continentino, Inorganic Chemistry **41**, 2193 (2002).

[36] J. B. Goodenough, *Magnetism and the Chemical Bond* (Interscience, New York, 1963).

[37] G. Ferey, M. Leblanc, R. Depape, and J. Pannetier, Solid State Communications **53**, 559 (1985).

[38] J. Bourgeois, G. Andre, S. Petit, J. Robert, M. Poienar, J. Rouquette, E. Elkaim, M. Hervieu, A. Maignan, C. Martin, and F. Damay, Physical Review B **86**, 024413 (2012).

[39] F. Damay, C. Martin, V. Hardy, A. Maignan, G. Andre, K. Knight, S. R. Giblin, and L. C. Chapon, Physical Review B **81**, 214405 (2010).

[40] J. Villain, Journal Of Physics And Chemistry Of Solids **11**, 303 (1959).

[41] M. Leblanc, G. Ferey, Y. Calage, and R. Depape, Journal of Solid State Chemistry **53**, 360 (1984).

[42] M. Leblanc, G. Ferey, P. Lacorre, and J. Pannetier, Journal of Magnetism and Magnetic Materials **92**, 359 (1991).

[43] J. C. Fernandes, R. B. Guimaraes, M. A. Continentino, H. A. Borges, A. Sulpice, J. L. Tholence, J. L. Siqueira, L. I. Zawislak, J. B. M. da Cunha, and C. A. dos Santos, Physical Review B **58**, 287 (1998).

[44] D. C. Freitas, M. A. Continentino, R. B. Guimaraes, J. C. Fernandes, E. P. Oliveira, R. E. Santelli, J. Ellena, G. G. Eslava, and L. Ghivelder, Physical Review B **79**, 134437 (2009).

[45] D. C. Freitas, M. A. Continentino, R. B. Guimaraes, J. C. Fernandes, J. Ellena, and L. Ghivelder, Physical Review B **77**, 184422 (2008).

[46] C. P. C. Medrano, D. C. Freitas, D. R. Sanchez, C. B. Pinheiro, G. G. Eslava, L. Ghivelder, and M. A. Continentino, Physical Review B **91**, 054402 (2015).

[47] D. C. Freitas, R. B. Guimaraes, D. R. Sanchez, J. C. Fernandes, M. A. Continentino, J. Ellena, A. Kitada, H. Kageyama, A. Matsuo, K. Kindo, G. G. Eslava, and L. Ghivelder, Physical Review B **81**, 024432 (2010).